Implementation of sub-grid scale temperature perturbations induced by non-orographic gravity waves in WACCM6

Simchan Yook[1]*, Susan Solomon[1], Michael Weimer[2],

Douglas E. Kinnison[3], Rolando Garcia[3], and Kane Stone[1]

Affiliations:

[1] Department of Earth, Atmospheric and Planetary Sciences, Massachusetts Institute of Technology, Cambridge, MA, USA

[2] Institute of Environmental Physics, University of Bremen, Bremen, Germany

[3] National Center for Atmospheric Research, Boulder, CO, USA

* Corresponding author. Email: syook@mit.edu

Key Points:

- We updated the subgrid-scale temperature parameterization to include non-orographic gravity waves from frontal activity and convection
- The non-orographic gravity waves increase the daytime variability of the ozone concentration, particularly in the lower mesosphere
- The non-orographic waves also enhance cirrus cloud formations in the upper troposphere across tropical to extratropical latitudes

Abstract:

Atmospheric gravity waves can play a significant role on atmospheric chemistry through temperature fluctuations. A recent modeling study introduced a method to implement subgrid-scale *orographic* gravity-wave-induced temperature perturbations in the Whole Atmosphere Community Climate Model (WACCM). The model with a wave-induced temperature parameterization was able to reproduce for example, the influence of mountain wave events on atmospheric chemistry, as highlighted in previous literature. Here we extend the subgrid-scale wave-induced temperature parameterization to also include *non-orographic* gravity waves arising from frontal activity and convection. We explore the impact of these waves on middle atmosphere chemistry, particularly focusing on reactions that are strongly sensitive to temperature. The non-orographic gravity waves increase the variability of chemical reaction rates, especially in the lower mesosphere. As an example, we show that this, in turn, leads to increases in the daytime ozone variability. To demonstrate another impact, we briefly investigate the role of non-orographic gravity waves in cirrus cloud formation in this model. Consistent with findings from the previous study focusing on orographic gravity waves, non-orographic waves also enhance homogeneous nucleation and increase cirrus clouds. The updated method used enables the global chemistry-climate model to account for both orographic and non-orographic gravity-wave-induced subgrid-scale dynamical perturbations in a consistent manner.

Plain Language Summary

Atmospheric gravity waves can affect atmospheric chemistry by inducing temperature changes. A recent study improved the Whole Atmosphere Community Climate Model (WACCM) to better account for these temperature changes caused by orographic gravity waves. Here we extend the method to also account for non-orographic gravity waves from frontal activity and convection. With this updated method, the model now simulates how these waves 1) influence chemical reactions in the middle atmosphere, as well as 2) affect cirrus cloud formation in the upper troposphere. The updated method allows the model to consistently incorporate the effects of both mountain-related and other types of gravity waves.

Main Text:

1. Introduction

Atmospheric gravity waves play an important role in the dynamical and thermal structure of the middle atmosphere (Holton 1983; Lindzen and Holton 1968; Andrews et al., 1987; Alexander et al., 2010). Gravity waves arise from different sources including orography, convection and jet/frontal systems, propagate both horizontally and vertically in a thermally stratified atmosphere, and transport horizontal momentum and energy from the troposphere to the middle atmosphere (Lilly and Kennedy 1973; Dörnbrack et al. 1999; Dewan et al. 1998; Piani and Durran 2000; O'Sullivan and Dunkerton, 1995; Fritts and Nastrom 1992a, b; Jiang et al. 2005). The acceleration resulting from the dissipation of the gravity waves (i.e., gravity wave drag) is one of the primary drivers of the large-scale circulation and affects transport of

chemicals in the middle atmosphere (Holton 1983; Lindzen and Holton 1968; Andrews et al., 1987; Garcia and Solomon, 1985; Alexander et al., 2010).

Gravity waves can also play a key role in photochemistry and microphysical processes in the atmosphere by changing atmospheric temperature and pressure. Wave-induced temperature fluctuations affect aerosol formation and growth (e.g., Peter et al. 1994; Meilinger et al. 1995; Borrmann et al. 1997; Tsias et al. 1997), polar stratospheric cloud formation (PSC; Carslaw et al. 1998a,b), cirrus cloud formation (Potter and Holton 1995; Jensen et al. 1996), and chemical reaction rates. This is because the chemical and microphysical processes exhibit strong non-linear dependence on temperature (e.g., Tabazadeh et al. 1994; Carslaw et al. 1994; Meilinger et al. 1995; Tsias et al. 1997). Cooling from wave-like temperature fluctuations can lead to cloud formation even though the mean temperature averaged across the wave motion remains above the cloud formation threshold. Several heterogeneous reactions, such as chlorine activation occurring on the surface of aerosol and PSCs (Borrmann et al. 1997), as well as gas-phase reactions, such as thermal decomposition of the ClO dimer (McKenna et al., 1990), are non-linearly dependent on temperature. Thus, net chemical rates can be significantly affected by gravity waves.

In general, current climate models still do not have enough horizontal resolution to explicitly simulate the mesoscale and smaller scale gravity waves. Thus, the main effects of the unresolved gravity waves on large-scale circulation need to be parameterized if they are to be included (Kim et al., 2003; Holt et al., 2016; Jewtoukoff et al., 2015). Several gravity wave schemes have been developed to represent sub-grid scale orographic gravity wave drag in different climate models (Alexander & Ortland, 2010; Alpert, 2004; Kim et al., 2003; McFarlane, 1987). Orographic gravity wave parameterization in Community Earth System Model (CESM) has been developed

based on the McFarlane theory, which assumes a two-dimensional steady-state hydrostatic wave with vertical propagation only (McFarlane, 1987). The CESM's orographic wave scheme has been improved to account for anisotropic orography including orientation, height, and size of orographic ridges (see appendix B in Weimer et al., 2023).

Gravity wave parameterizations have also been developed to represent non-orographic gravity waves generated by two dominant sources: 1) convectively generated gravity waves based on the theoretical relationship between convective heating and wave momentum fluxes (Beres et al., 2004; 2005; Bushell et al., 2015; Chun et al., 2008), and 2) frontally generated gravity waves using the frontogenesis function (Hoskins 1982) as a diagnostic for wave momentum flux induced by frontal activity (Charron and Manzini, 2002; Richter et al., 2010; Richter et al., 2014).

In global climate models, implementing the unresolved gravity wave perturbations in chemical and microphysical processes has been considered challenging; however, some studies have developed parameterizations of the sub-grid scale perturbations on cirrus formation (Dean et al., 2007; Barahona et al., 2017; Penner et al., 2018; Lyu et al., 2023), as well as PSC formation and middle atmospheric chemistry (Orr et al., 2020; Weimer et al., 2021, 2023).

Two recent studies, Weimer et al. (2023) and Lyu et al. (2023), developed a similar method to account for the temperature and vertical velocity fluctuations induced by sub-grid scale gravity waves in the Community Earth System Model version 2 (CESM2; Danabasoglu et al., 2020). They both estimated the amplitude of wave-induced fluctuations based on parameterized wave momentum fluxes from *orographic* gravity-wave schemes and grid-scale dynamical fields (temperature and wind fields). Weimer et al. (2023) converted the sub-grid scale wave momentum flux to temperature fluctuations and included them in the chemistry, and Lyu et al.

(2023) applied the vertical velocity fluctuations to the microphysics of cirrus cloud formation. While Weimer et al. (2023) and Lyu et al. (2023) mainly focused on the role of orographic waves, it has been suggested that gravity waves originating from non-orographic sources can also play an important role in global atmospheric circulation, as well as in chemical and microphysical processes (e.g., Kärcher & Ström, 2003; Schoeberl et al., 2016; Dinh et al., 2016; Wright, 2019; Zou et al., 2021).

Building on the method from previous studies, we aim to account for the sub-grid scale dynamical fluctuations induced by gravity waves from different sources including *non-orographic* gravity waves arising from frontal activity and convection. Then, we explore examples of their role in global atmospheric modeling. Section 2 describes the model, experiments, and method to estimate the amplitude of sub-grid scale temperature fluctuations. Section 3 explores the impacts of the gravity waves on example chemical concentrations and ice clouds. Section 4 summarizes the results and discusses future implications.

2. Method

2.1. WACCM6

The Whole Atmosphere Community Climate Model (WACCM6) of the Community Earth System Model (CESM2.1) is used in this study (Danabasoglu et al., 2020; Gettelman et al., 2019). The FWSD compset (refer to Gettelman et al., 2019) based on the Specified Dynamics (SD) version of the model (Davis et al., 2022) with a relaxation time of 50 hours is used following Weimer et al. (2023). Thus, in all experiments, the modeled winds and temperatures between the surface to 1 hPa are relaxed toward reference meteorology from Modern-Era Retrospective Analysis for Research and Applications version 2 (MERRA2, Gelaro et al., 2017). The chemistry scheme for WACCM includes detailed chemistry for the Troposphere,

Stratosphere, Mesosphere and Lower Thermosphere (TSMLT scheme) and includes 158 photochemical species, 117 photolysis reactions, 331 gas-phase reactions, 2 aqueous-phase reactions, and 10 heterogeneous reactions (Mills et al., 2016; Marsh et al., 2013; Emmons et al., 2020; Kinnison et al., 2007). The SD-WACCM simulations are run with a horizontal resolution of 1.25° × 0.9°, 88 vertical levels, a model top at about 140 km, and prescribed ocean and ice models.

2.2. Parameterization of non-orographic gravity waves in WACCM6

The non-orographic gravity wave parameterization in WACCM6 includes separate source specifications of convective and frontal gravity waves (Richter et al., 2010; Gettelman et al., 2019). The convective gravity wave parameterization employs the "Beres scheme" to specify the gravity wave source spectrum (Beres et al., 2004; Beres et al., 2005). The model's deep convection parameterization scheme (Zhang & McFarlane, 1995) provides information about the depth and rate of convective heating, and then the phase speed spectrum of gravity wave momentum flux is determined by the Beres scheme based on the convective heating rate and the mean horizontal wind in the heating region. Thus, the convective gravity wave source specification in WACCM6 is coupled to the model's internal representation of convective processes. The convective gravity waves generated by the Beres scheme in WACCM6 were validated using tropical observations (Alexander et al., 2023).

The frontal gravity wave source specification is based on the frontogenesis function (Miller 1948; Hoskins 1982). At each time step, the frontogenesis function is calculated using information about the dynamical fields at a 600 hPa level, which corresponds to a typical steering level of fronts (Charron and Manzini, 2002). Then, the frontal gravity waves are

158 launched in all grid points where the frontogenesis function at 600 hPa exceeds a specific
159 threshold (Richter et al., 2010).

160 **2.3. Sub-grid scale dynamical fluctuations due to gravity waves**

161 We provide a brief summary of the subgrid-scale temperature parameterization and the
162 sub-stepping method (for details see Weimer et al., 2023). The peak wave displacement
163 amplitude ($\hat{\delta}$) is calculated based on the wave properties, including wave momentum flux (τ),
164 phase speed, and wavelength derived from the wave drag scheme and other information about
165 the background dynamical fields as follows (Lindzen, 1981),

166 $$\hat{\delta} = \sqrt{\frac{\tau}{\rho N |\overline{U} - c| k_h}}, \quad (1)$$

167 where $\rho, N, \overline{U}, c$ and k_h denotes air density, the Brunt-Vaisala frequency, horizontal wind speed,
168 wave phase speed, and the horizontal wave number, respectively. Then, the amplitude of
169 temperature fluctuation ($\hat{T}$) by the subgrid-scale gravity wave is estimated using the peak wave
170 displacement amplitude as follows,

171 $$\left|\hat{T}\right| = S\hat{\delta}, \quad (2)$$

172 where S denotes the static stability.

173 Our method for estimating temperature fluctuation closely follows that outlined in
174 Weimer et al. (2023), except for the following differences in how we estimate the total
175 momentum flux. For orographic waves, Weimer et al. (2023) used a single vertical wavenumber
176 component corresponding to the largest amplitude to estimate the peak wave displacement.
177 However, for non-orographic gravity waves, we used a full spectrum of vertical wavenumbers
178 after applying few simplifications. Although it is well known that complex wave-wave

interactions among waves with different wavenumbers significantly influence the shape and evolution of the total gravity wave spectrum (Fritts and Alexander, 2003), we simplify the total momentum flux of the wave spectrum by summing momentum fluxes over a phase speed spectrum in each cardinal direction, and then selecting the direction with the highest magnitude. The peak wave displacement ($\hat{\delta}$) is calculated using the total momentum flux (τ) at each grid point, together with the vertical wavenumber corresponding to the maximum momentum flux in the spectrum and background dynamical fields. We acknowledge that our calculations involve certain simplifications, such as selecting a single vertical wavenumber corresponding to the maximum momentum flux, rather than accounting for the superposition of different wavenumbers. The results are not sensitive to the simplification of using a single vertical wavenumber corresponding to the maximum momentum flux instead of the full spectrum of phase speeds, for the peak wave displacement calculation (Fig. S1). In future work, applying a scaling approach similar to that in Weimer et al. (2023) by comparing with observations could help reduce model biases in the amplitude of wave-induced temperature fluctuations.

Following Lyu et al. (2023), we estimate subgrid-scale vertical velocity variances (σ_w^2) as below,

$$\sigma_w^2 \sim (k_h|\overline{U} - c|\hat{\delta})^2. \quad (3)$$

For calculating the subgrid-scale vertical velocity variances, we also adopted Lyu et al.'s (2023) modification of setting the horizontal wavelength to 10 km as a scaling factor, as well as their approach for implementing the wave-induced vertical velocity variance in the second version of the two-moment Morrison and Gettelman microphysics scheme (MG2; Gettelman et al., 2010, 2019; Gettelman & Morrison, 2015).

The wave-induced 1) temperature perturbations and 2) vertical velocity variances are estimated individually for each gravity wave source (orographic, convective, and frontal). The perturbation with the largest amplitude is then selected at each grid point to represent the peak amplitude of temperature fluctuations ($|\widehat{T}|$) and total wave-induced vertical velocity variances. We note that the different types of gravity wave perturbations from each wave source can be used together or separately, by specifying the corresponding CESM namelist variables. The wave-induced fluctuations are limited to inputs for the chemistry module and the MG2 microphysics scheme but are not incorporated into the model's resolved dynamical fields.

2.4. Sub-stepping method and stochastic approach

Using information about the temperature fluctuations, we applied the sub-stepping method to the chemistry module as follows: the time evolution of temperature fluctuation is assumed to have a form of sine wave with an estimated amplitude of $|\widehat{T}|$ and a period of one model time step (30 minutes); the temperature for the chemistry is sampled at 10 intermediate sub-time steps (every 3 minutes); and the chemistry and associated processes are updated with the changing temperature at each sub-time step to represent the changes in multiple chemical species as the wave-induced temperature fluctuations evolve. The limitation of choosing 30 minutes as the wave intrinsic period was discussed in Weimer et al. (2023), and a 30-minute wave period could be reasonable under limited conditions (e.g., strong background wind conditions for mesoscale gravity waves, such as those in the polar vortex).

Weimer et al. (2023) have developed an alternative way of simulating wave-driven temperature perturbations other than the sub-stepping method: a stochastic approach using sine-

wave-distributed random $|\widehat{T}|$. In the stochastic approach, the phase of the wave is chosen as a random variable between -π/2 and π/2 to simulate various phases of gravity waves at each model time step (for details, see Section 2 in Weimer et al., 2023). Stochastically selecting $|\widehat{T}|$ at each model time step (30 minutes) is equivalent to assuming that the intrinsic period of the wave is equal to or greater than 30 minutes. Since the stochastic approach does not involve any sub-stepping, it can reduce computational costs while reproducing similar results compared to the sub-stepping method in long-term statistics. In this study, we confine the analysis to the sub-stepping method to assess changes in chemistry occurring over a time scale of a few hours; however, the stochastic approach is also available as an alternative option for future studies. For example, it can be used to examine the influence of different initial phases of wave-induced perturbations on chemical species at the model's dynamical time step.

2.5. Experiments

We ran two sets of historical experiments, one implementing the sub-grid scale non-orographic gravity wave perturbations on the chemistry through sub-stepping (GW), and another reference simulation without the sub-grid scale wave parameterizations (REF). To highlight the influence of non-orographic gravity waves, we set the scaling factor for temperature perturbations induced by orographic waves to zero in the GW runs. However, as mentioned in an earlier section, temperature perturbations from different types of wave sources can be used together or separately, depending on the research focus. We chose to analyze the year 2007, following Weimer et al. (2023). The sub-stepping is also applied in the REF simulation but without temperature fluctuations in order to maintain consistency with the GW simulation by accounting for any variability that may be due to the sub-stepping process itself. The chemistry

responses to sub-grid scale gravity wave parameterizations are dependent on internal climate variability. Here we use 5 ensemble members for each set of experiments, run with slightly different initial dates ranging from December 15, 2006 to December 23, 2006 with two days interval, to isolate the signatures of gravity waves from other forms of internal climate variability. All ensemble members were integrated until December 31, 2007.

We also run another experiment (MG2-GW) applying wave-induced vertical velocity fluctuations to the MG2 scheme, following Lyu et al. (2023). In the MG2-GW runs, configurations other than the vertical velocity fluctuations were identical to the REF runs (i.e., the temperature perturbations were set to zero) to highlight the difference arising from the vertical variance perturbations only. The MG2-GW runs were integrated for four months, from January 1, 2007, to April 30, 2007, as we focus on demonstrating any changes occurring on a seasonally averaged time scale.

3. Results

We present the global distribution of gravity wave-induced temperature perturbations, $\hat{T}$, in Figure 1. We first consider the maximum value of daily-mean $\hat{T}$ from all five ensemble members of the GW simulation. The amplitude of temperature fluctuations increases with height at all latitudes, as atmospheric density decreases (Fig. 1a). Temperature fluctuations are pronounced over the extratropical latitudes, with large amplitudes of approximately 15 K estimated at 0.14 hPa level. These temperature fluctuation patterns over the extratropics indicate significant contributions by waves generated from frontal systems (Figs. 1b; Figs. S2a-c). At the tropical latitudes, temperature perturbations are particularly pronounced over the western Pacific warm pool region as well as the eastern equatorial Pacific, reaching maximum amplitudes of ~5

K at 15 hPa level. This suggests a major influence of waves generated by convective heating sources (Fig. 1c; Figs. S2d-f). While non-orographic gravity waves exhibit some features over the mountains (likely amplified due to significant orographic precipitation biases in CESM, as reported in previous studies; Sakaguchi et al., 2018; Reboita et al., 2024), they also exhibit pronounced signatures over the tropical latitudes and over the ocean (Fig. 1), where the influences of orographic waves were limited or zero (see Figs. 2 and 7 in Weimer et al., 2023). Thus, the results in Fig. 1 suggest that non-orographic waves need to be accounted for to achieve a more realistic representation of the wave-induced temperature variability.

The results presented here are based on temperature fluctuations internally generated by the model, without any additional scaling applied to compare with observations. This is because the amplitudes of temperature fluctuations induced by non-orographic waves are poorly constrained quantities on a global scale, as it is challenging to distinguish non-orographic from orographic wave influences in observations. Thus, in practice, the amplitudes of fluctuations can be considered as parameters that can be tuned to the extent observations are available. We note that new datasets, based on observations from satellites and superpressure balloons, have recently become available, offering comprehensive statistics on temperature fluctuations associated with both orographic and non-orographic gravity waves (Ern et al., 2018; Hindley et al., 2020; Corcos et al., 2021; Bramberger et al., 2022). Future investigations could include comparisons with observations using both orographic and non-orographic parameterizations.

We next explore the influences of gravity waves on middle atmosphere chemistry, particularly focusing on ozone concentrations, which are known to be strongly sensitive to temperature in the upper stratosphere and lower mesosphere (Barnett et al., 1975; Prather, 1981; Brasseur and Solomon, 2005). Figure 2 reveals ratios of variance in daily minimum ozone

concentrations between the GW and REF runs. The daily minimum ozone value reflects the lowest instantaneous ozone concentration occurring at the sub-stepping time scale (3 minutes). All available time steps based on five ensemble members from each simulation are used to calculate the variances; thus, the variances are estimated over 5 ensemble members X 31 days X 288 longitudinal grid points = 44640 samples for Figure 2a, and over 165 samples (5 ensemble members X 31 days) for Figure 2b. The F statistic is used to assess the statistical significance of the ratios between variances ($p < 0.05$). The seasonal cycle was not removed in order to highlight regions where changes in variability due to waves exceed the amplitudes of variation following the seasonal cycle during the analysis period. We analyze July 2007, but the results are not sensitive to a specific period as similar results were found from August to October of the same year (not shown).

We focus on the daily minimum ozone concentration for the following reasons. Observational and modeling studies have shown that the diurnal cycle of ozone above ~1 hPa is characterized by substantially smaller daytime ozone concentrations compared to nighttime concentrations (Lean, 1982; Haefele et al., 2008; Huang et al., 2008; Sakazaki et al., 2013; Schanz et al. 2014). This is because the ozone distribution in that region can be described by ozone photochemistry in a pure oxygen atmosphere (i.e., the Chapman mechanism), where the daytime ozone concentration is smaller than the nighttime concentration due to photolysis by UV light (Chapman, 1930; Prather, 1981; Brasseur and Solomon, 2005). Some photochemical reactions in the Chapman mechanism (e.g., the recombination of atomic oxygen and ozone), which are highly temperature-sensitive, occur primarily during the daytime. Thus, to investigate the influence of gravity waves on ozone variability, we focus on minimum ozone concentration during daytime and its sensitivity to the wave-induced temperature variations.

315 The key result in Figure 2a is that the non-orographic gravity waves increase the
316 variability of daily minimum ozone concentrations in the lower mesosphere between ~0.3 hPa
317 and 0.07 hPa around 60^{o}N. In Figure 2b, we focus on a single pressure level (0.14 hPa) to
318 exclude the influences of the variances arising from the longitudinally asymmetric component of
319 the ozone distribution. At the 0.14 hPa level, local variances of daily minimum ozone increase by
320 a factor of up to ~2 over the North Pacific (Fig. 2b).

321 We further explore the connection between changes in chemistry and gravity wave
322 temperature fluctuations. Figure 3 exhibits the time series of daily minimum ozone
323 concentration, daily mean wave-induced temperature fluctuations, and daily mean temperature,
324 focusing on a specific grid point representing a hot spot of frontal gravity wave activity near the
325 North Pacific. Figure 3a reveals an average decrease of roughly ~13 ppbv in the daily minimum
326 ozone concentration in the GW runs compared to the REF runs during the first 10 days of July.
327 The difference in minimum ozone concentrations between the GW and REF runs (i.e., difference
328 between red and blue lines) in early July is also larger than the internal variability among
329 different ensembles (i.e., the red or blue shading).

330 More importantly, substantial increases in sub-grid scale temperature fluctuations are also
331 shown over the periods that correspond to significant differences in the minimum ozone
332 concentrations in the two experiments (Figs. 3a and 3b). The amplitudes of $\hat{T}$ (> ~5 K) are larger
333 than changes due to the internal variability of daily-mean temperature, and thus can have some
334 local effects on strongly temperature dependent chemical reactions. Larger decreases in
335 minimum ozone concentration are revealed in the sensitivity experiments run with larger
336 amplitudes of temperature perturbations (with scaling factor=$\sqrt{3}$; Fig. S3), further suggesting a

337 causal relationship between them. In the following section, we explore the influences of waves
338 on the ozone concentration and chemical reactions exhibiting temperature dependency.

339 Figure 4 presents timeseries of ozone concentration, wave-induced temperature
340 fluctuations, and reaction rates that drive ozone chemistry at the same location over the North
341 Pacific as in Figure 3 but focusing on 2-hour intervals around the time when the daily minimum
342 ozone occurs. The results in Figure 4 are based on an additional experiment run with the same
343 configuration as in the GW runs, but the integration was started from June 21, 2007, and the
344 variables were outputted at a higher frequency (3-minute intervals) to investigate the influences
345 of waves on the fluctuations in ozone concentration.

346 Black dots in Fig. 4a indicate instantaneous ozone mixing ratio outputted at each sub-
347 time step. The ozone mixing ratio shows a nearly sinusoidal oscillation with a period of 30
348 minutes (which is equal to one sub-stepping cycle and the WACCM dynamical time step) and a
349 peak-to-peak amplitude of ~60 ppbv on July 2, 2007 (Fig. 4a). This oscillation in ozone
350 concentration is shown only in the GW runs, not in the REF runs (Fig. S4a), which in turn leads
351 to increases in the daytime ozone variability in the GW runs, compared to variability in the REF
352 runs (Figs. 3a and S4a). It is noteworthy that satellite measurements with sufficient temporal and
353 horizontal resolution may be able to sample variations in ozone comparable to these chemical
354 changes over the wave-induced fluctuations.

355 Ozone concentrations (Fig. 4a) and temperature perturbations (Fig. 4b) are anti-correlated
356 with each other. To assess the cause of the relationship between the ozone concentration and
357 temperature, we first identify the chemical reactions that are primary drivers of the ozone
358 variations, and then explore their temperature dependencies. Red dots in Fig. 4c represent
359 ozone's chemical tendency estimated as a sum of the three-body recombination reaction rate

(Fig. 4d), ozone's photolysis rate (Fig. 4e), atomic oxygen-ozone recombination rate and ozone-hydrogen reaction rate (Fig. 4f). These processes in Figs. 4d-f are known to be the dominant ozone sources and sinks in the lower mesosphere (Brasseur and Solomon, 2005).

Red dots in Fig. 4a are shown to compare the ozone concentration calculated by the time integration of the net chemical tendency mentioned above (Fig. 4c), with the actual ozone concentration time series (black dots in Fig. 4a). Again, the ozone's chemical tendency is estimated as the sum of the chemical rates shown in Figs. 4d-f. The integration starts from the initial ozone concentration at local time 17:30 to avoid potential long-term drift due to dynamical transport and chemical losses from reactions not included in the calculation. We note that the absence of dynamical tendency (green dots in Figs. S4e-f) and chemical losses from other reactions (red dots in Figs. S4e-f) can accumulate errors in the predicted ozone concentration when integrated over time (Fig. S4d). However, we consider these errors are negligible in our 30-minute analysis interval (i.e., within a sub-stepping cycle).

What are the main drivers of the simulated ozone variations? Close similarity between red and black dots in Fig. 4a highlights that the calculation based on the net chemical rate captures most of the simulated ozone variations. Thus, the results in Fig. 4a confirm that changes in ozone concentration are largely driven by the processes listed in Figs. 4d-f, with the three-body recombination reaction (Fig. 4d) and photolysis (Fig. 4e) respectively being the main source and sink of ozone at this location given their large amplitudes.

We now explore the temperature dependencies of the photochemical reactions in Figs 4d-f. Both the rates of ozone production (Fig. 4d) and the photolysis (Fig. 4e) display distinct oscillatory pattern as well as an out-of-phase relationship with the temperature perturbation (Figs. 4b, d, and e). This temperature dependencies of ozone reaction rates are due to the

383 combined effects of 1) the temperature dependency of reaction rate coefficients and 2) the
384 temperature induced air density variations, following the ideal gas law (Chapman, 1930; Prather,
385 1981; Brasseur and Solomon, 2005; Lean 1982). The temperature dependencies of ozone
386 photochemistry (Figs. 4d-f), in turn, lead to oscillatory behavior in the net ozone tendency (Fig.
387 4c), as the net changes in ozone are governed by a balance between these processes. Together,
388 the results in Fig. 4 reveal that the gravity wave-induced temperature perturbations 1) cause the
389 sinusoidal oscillation in the ozone mixing ratio, and 2) lead to increases in the daytime ozone
390 variability in the GW runs compared to the variability in the REF runs.

391 Figure 5 exhibits the vertical structure of changes in ozone mixing ratio (Fig. 5a,
392 production rate (Fig. 5b), and loss rate (Fig. 5c) during a sub-stepping cycle between local time
393 18:30-19:00 between 1 and 0.05 hPa. The red, black, and blue lines represent values
394 corresponding to the maximum, zero, and minimum during a cycle of the wave, respectively.
395 Large variations in the ozone mixing ratio and chemical rates are obtained above the ~0.2 hPa
396 level. The results here indicate that the increase in daily minimum ozone in the GW runs shown
397 in Figure 2 is primarily due to the wave-induced temperature fluctuations that affect the
398 temperature-dependent chemical rates involved in ozone chemistry, which in turn lead to
399 increases in daily ozone variability. Together, the results in Figs. 2-5 demonstrate an example of
400 many instantaneous processes associated with sub-grid scale gravity wave activity that were not
401 simulated in the standard version of WACCM simulations. This highlights the role of sub-grid
402 scale waves on atmospheric chemistry.

403 The role of non-orographic gravity waves in cirrus cloud formation is briefly summarized
404 in Figure 6 as another implication of gravity wave perturbations in climate modeling. In
405 WACCM6, the MG2 scheme predicts ice nucleation in cirrus cloud formation using sub-grid

406 vertical velocity variances. In the default setting, the vertical velocity variances are associated
407 with the amplitudes of sub-grid scale turbulent motion derived from CLUBB (Cloud Layers
408 Unified by Binormals; Golaz et al., 2002a, 200b). Here, we also estimated sub-grid vertical
409 velocity variances associated with convective and frontal gravity waves and introduced them into
410 the ice nucleation parameterization.

411 Figs. 6a, 6c, and 6e compare the sub-grid scale vertical velocity variances for the ice
412 nucleation parameterization between the MG2-GW and REF simulations. Both runs show high
413 values of the vertical velocity variances over tropical latitudes, consistent with a previous study
414 based on 7-km high-resolution modeling (Barahona et al., 2017). Vertical velocity variances are
415 increased in the upper troposphere over the tropical and extratropical latitudes (60°S-60°N) with
416 inclusion of the wave-induced vertical velocity fluctuations (Fig. 6e). As expected, cloud ice
417 mixing ratio also increases in the same regions (Fig. 6f), suggesting that the onset of ice
418 supersaturation is triggered by the sub-grid scale gravity waves. Our results highlight that the
419 influence of non-orographic waves is pronounced over tropical and extratropical latitudes in the
420 upper troposphere. This finding is consistent with a previous study based on observational
421 analyses and trajectory modeling (Schoeberl et al., 2016), which found that gravity waves
422 increase the upper tropical tropopause cloud fraction. Another study based on numerical
423 simulations using balloon-observed temperature data (Dinh et al., 2016) also suggests that high-
424 frequency temperature fluctuations due to gravity waves can control the homogeneous nucleation
425 of cloud ice in the vicinity of the tropical tropopause.

426 We find that the main results presented here (scaling factor=1; Figs. 2,3, and 6) remain
427 qualitatively similar to results from the sensitivity experiments run with larger amplitudes of
428 wave-induced perturbations (scaling factor=$\sqrt{3}$; Figs. S3, S5 and S6).

Summary and Conclusions

Recent modeling studies introduced a method to account for the effects of subgrid-scale *orographic* gravity-wave-induced dynamical perturbations in community climate models: 1) temperature perturbations on the atmospheric chemistry in WACCM6 (Weimer et al., 2023), and 2) vertical velocity perturbations on cirrus cloud formations in CAM6 (Lyu et al., 2023). The methods estimate the dynamical perturbations of gravity waves based on the model's gravity wave parameterizations and introduce them into the chemistry module and microphysics scheme (respectively). Here we extended the method to also include perturbations by *non-orographic* gravity waves arising from frontal activity and convection. The sub-grid scale temperature fluctuations are estimated in a similar manner to the method outlined in Weimer et al. (2023), except that the momentum fluxes were calculated based on a wave spectrum instead of a monochromatic wave. We integrated momentum fluxes over a phase speed spectrum to estimate the total wave momentum flux from different wavenumbers and used the results to calculate peak wave displacement amplitudes. The wave-induced fluctuations were then applied to chemistry as a sine-wave perturbation using a time interval sub-stepping method. Similarly, sub-grid vertical velocity perturbations were derived following the method by Lyu et al. (2023), and then applied to the MG2 scheme for the ice nucleation parameterization.

Two sets of 1-year long simulations were conducted with WACCM6: one based on the default WACCM6, and a second one with the sub-grid scale gravity wave perturbations. We compared the simulation in the two experiments to assess the global pattern of temperature fluctuations induced by non-orographic waves, as well as the role of wave-induced dynamical

perturbations on an example case of middle atmosphere chemistry and cirrus cloud formation in the upper troposphere. The key implications of the method are as follows:

1) The non-orographic gravity waves increase the variability of chemical reaction rates, particularly in the upper stratosphere and lower mesosphere, which, in turn, leads to an increase in the daytime variability of the ozone concentration.

2) The non-orographic waves also enhance homogeneous nucleation and thus increase cirrus clouds in the upper troposphere across tropical to extratropical latitudes.

Our method provides estimates of the amplitudes of the temperature perturbations based on WACCM's internal physics and parameterizations. This has various possible implications for climate and chemistry. Convective gravity waves are known to play an important role in the cold point tropopause temperature as well as stratospheric water vapor abundances (Jensen and Pfister, 2004; Kim and Alexander, 2013; 2015). While beyond the scope of the current work, our method could be used to address the effects of sub-grid scale gravity waves on the variability of simulated cold point temperatures. Future work could also compare the detailed statistics of simulated wave-induced temperature fluctuations, such as amplitudes, frequencies, and spatial patterns, with the characteristics of observed gravity waves on a global scale.

Acknowledgments: S. S and S. Y. are supported by grant AGS-1906719 from the Atmospheric Chemistry Division of the U.S. National Science Foundation (NSF). The CESM project is supported by the NSF and the Office of Science (BER) of the U.S. Department of Energy (DOE). The authors acknowledge the Climate Simulation Laboratory at NCAR's Computational and Information Systems Laboratory (CISL; sponsored by NSF and other agencies) for providing computing and storage resources that have contributed to the research results reported within this

paper. The authors thank Petr Šácha and two anonymous reviewers for their helpful comments on the manuscript.

Open Research

(dataset) The dataset used in the generation of the figures of this paper are available at (Yook, 2024).

(software) The model code modifications to add the parameterization to the published version of CESM2.1.4 (see Danabasoglu et al., 2020) can also be found at (Yook, 2024).

Figures

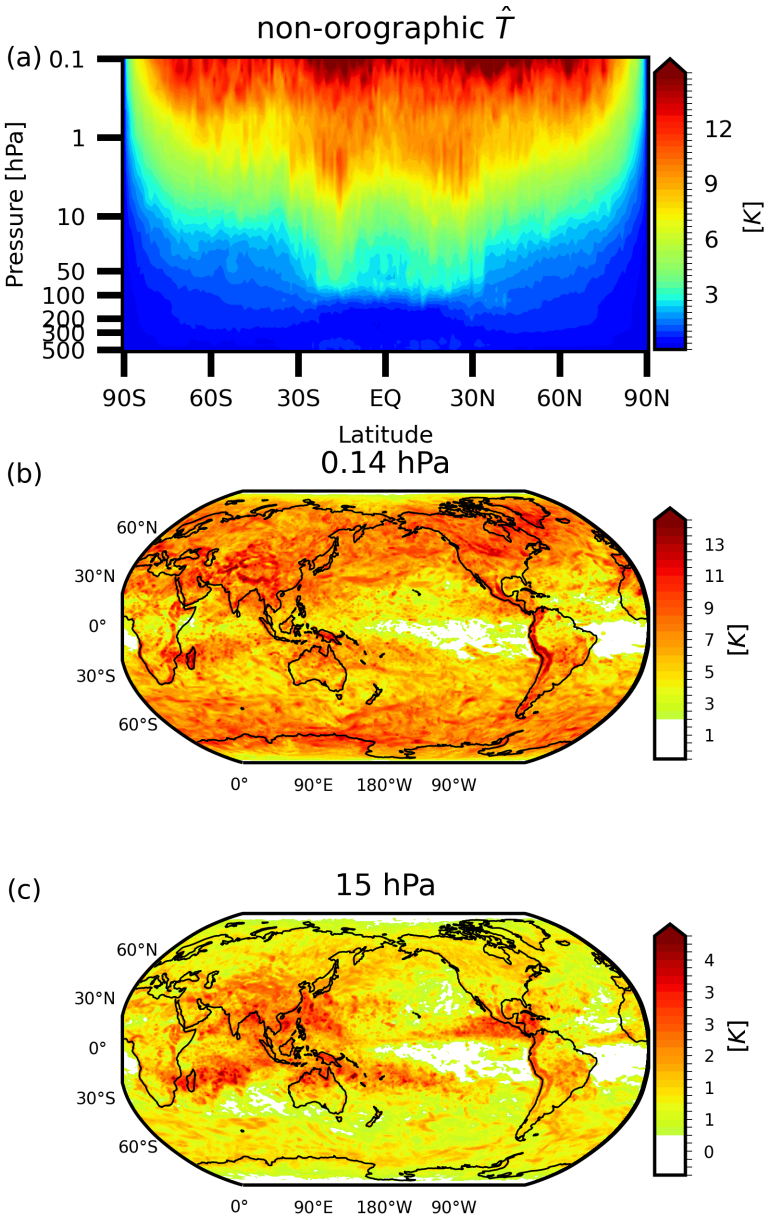

Figure 1. Maximum values of daily mean $\hat{T}$ in 2007 for the "non-orographic gravity wave" (GW) runs. The results displayed are the maximum value of all grid points as a function of latitude (top), maximum value at each grid point at the 0.14 hPa level (middle), and 15 hPa level (bottom).

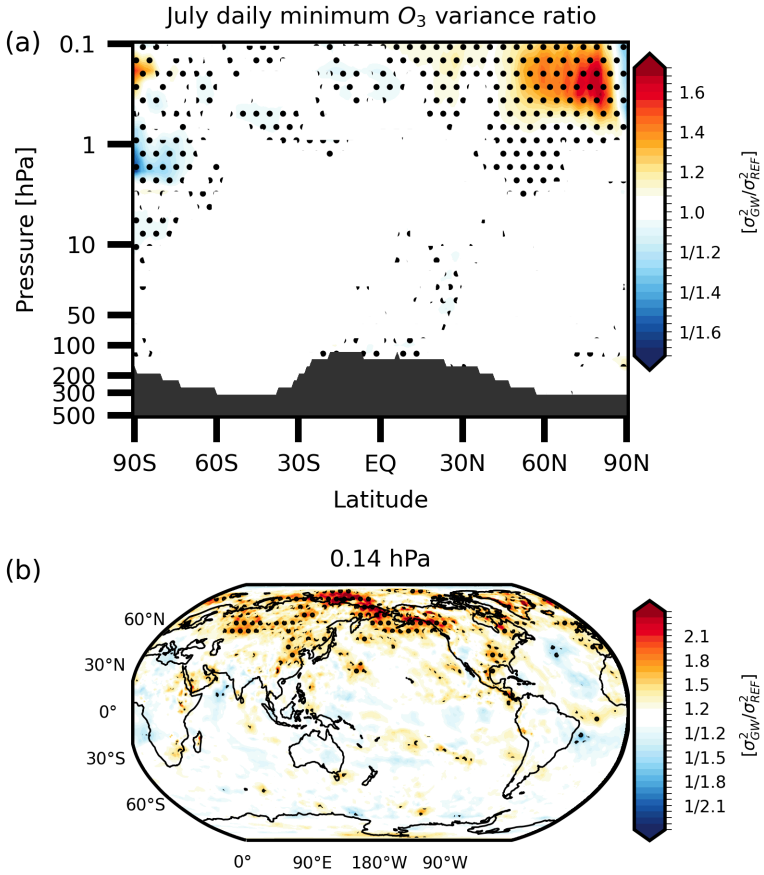

503

504 **Figure 2.** Ratio of the variance in daily minimum ozone concentration between GW and REF
505 runs. The results displayed are the daily minimum values in all grid points as a function of
506 latitude (top) and values at each grid point at the 0.14 hPa level (bottom) in July 2007. Note the
507 non-linear color scale in both panels. Regions within the troposphere are masked out in the upper
508 panel. Stippling indicates regions where the ratios exceed the 95% threshold.

509

510

511

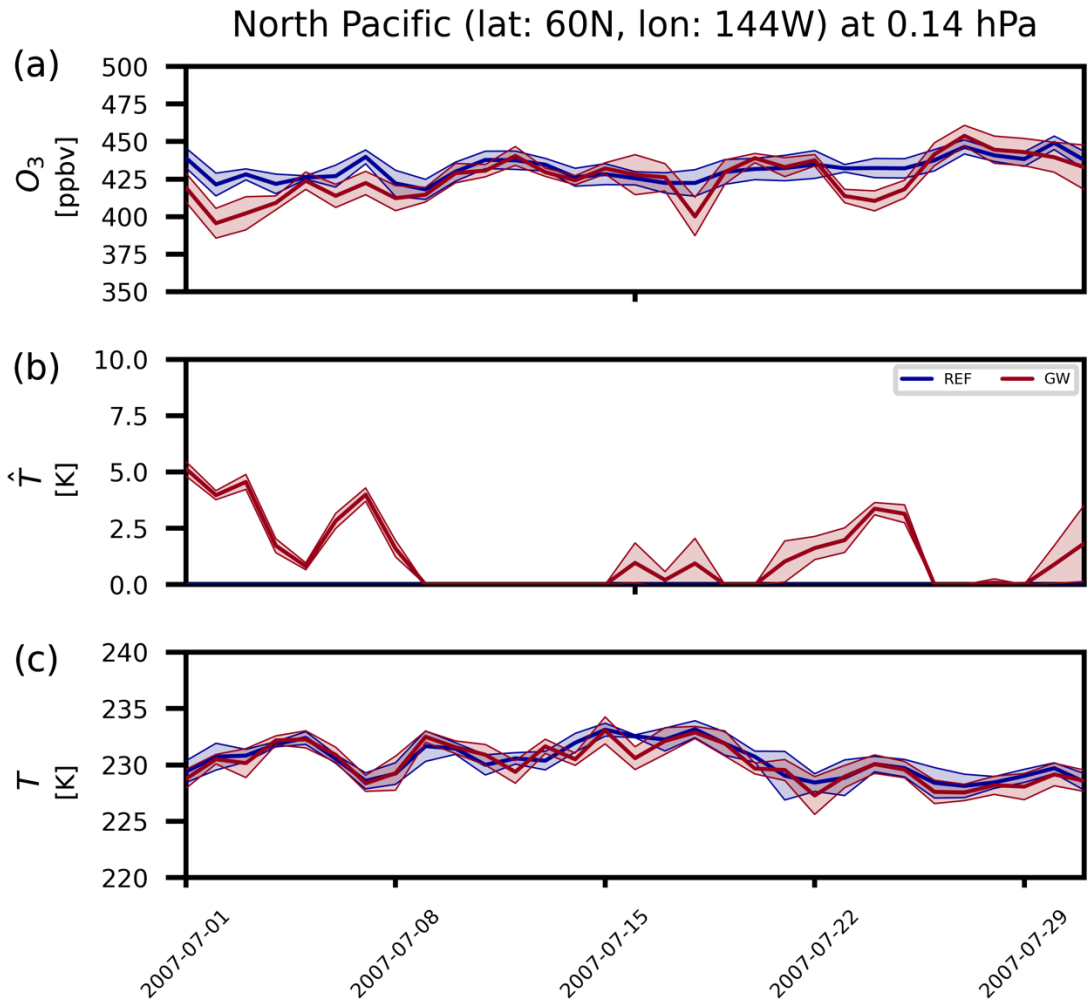

512

513 **Figure 3.** Timeseries of daily minimum concentration of ozone (top), daily mean wave-induced
514 temperature perturbation (middle), and daily mean temperature (bottom) at a single WACCM
515 grid point over the North Pacific (144°W, 60°N) at 0.14 hPa level. Each colored line and range
516 represents the results based on the ensemble mean and spread of the (red) GW and (blue) REF
517 runs. The spread is defined as one standard deviation among ensemble members for each field on
518 each day.

519

520

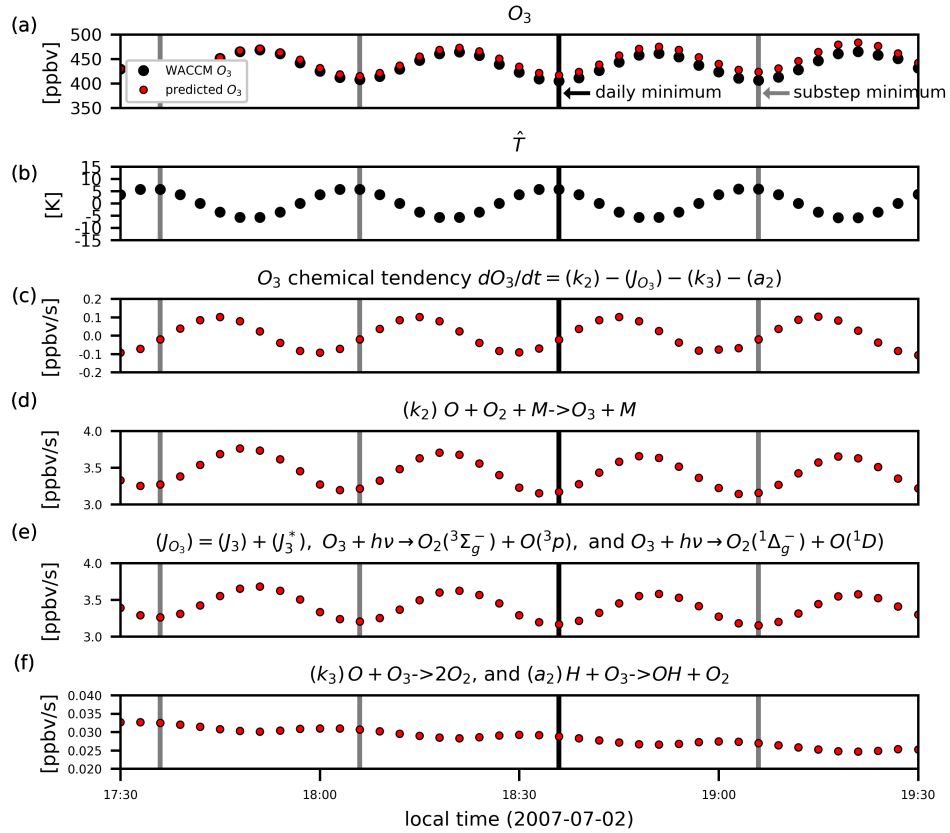

Figure 4. Timeseries of daytime (a) ozone concentration, (b) wave-induced temperature perturbation, (c) net chemical rate for ozone, (d) three-body recombination reaction rate, (e) ozone photolysis rate (the sum of two indicated pathways producing O^3P and O^1D, respectively), and (f) atomic oxygen-ozone recombination rate and ozone-hydrogen reaction rate. Black dots in panel (a) indicate the instantaneous ozone mixing ratio, while red dots represent the corresponding values estimated based on the sum of chemical rates in rows d-f. All results are instantaneous values sampled at 3-minute intervals. The timing for the absolute daily minimum ozone is indicated by black shading and timings for relative minimum values in each sub-step

cycle are marked by gray shading. All reaction rate coefficients, k_i, and photolysis rates, J_i, followed the notation used by Brasseur and Solomon (2005). The results are derived from the same location over the North Pacific as in Figure 3.

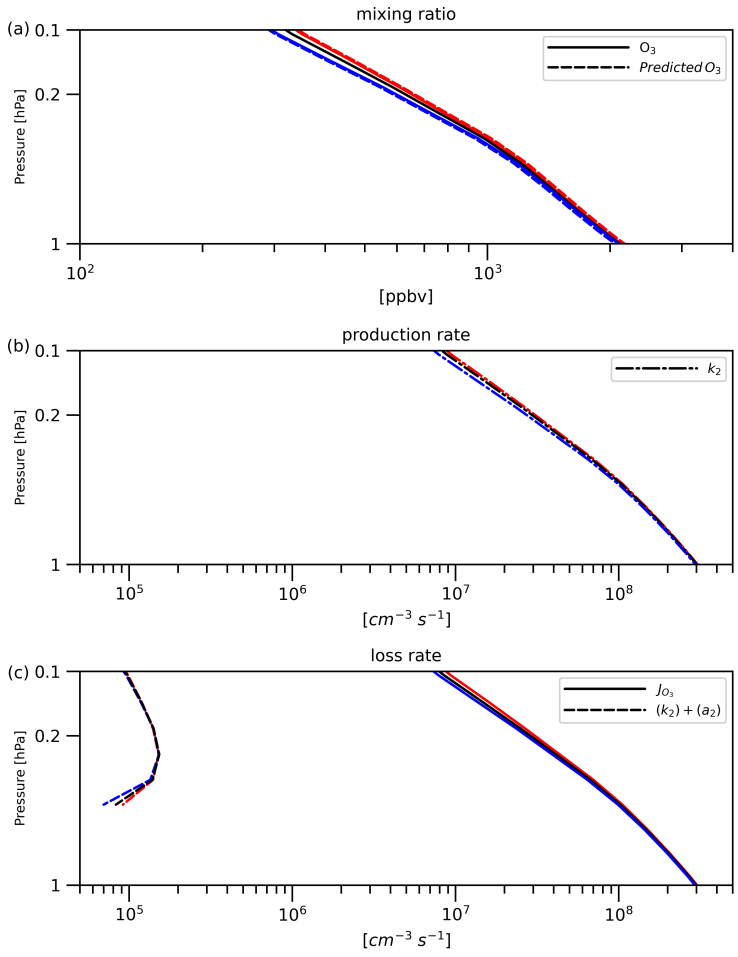

Figure 5. Vertical profile of ozone's (a) mixing ratio, (b) production rate, and (c) loss rate during a sub-stepping cycle between local time 18:00-19:00. The results are derived from the same location over the North Pacific as in Figures 3-4. The red, black, and blue lines represent values corresponding to the maximum, zero, and minimum displacement phase, respectively. The dashed-dotted line in panel (b) shows the three-body recombination rate, the solid line in panel (c) exhibits the photolysis rate, and the dashed line in panel (c) exhibits the sum of atomic

544 oxygen-ozone recombination rate and ozone-hydrogen reaction rate. Dashed lines in panel (a)
545 show predicted ozone abundances based on the net chemical rates defined as the sum of the three
546 processes.

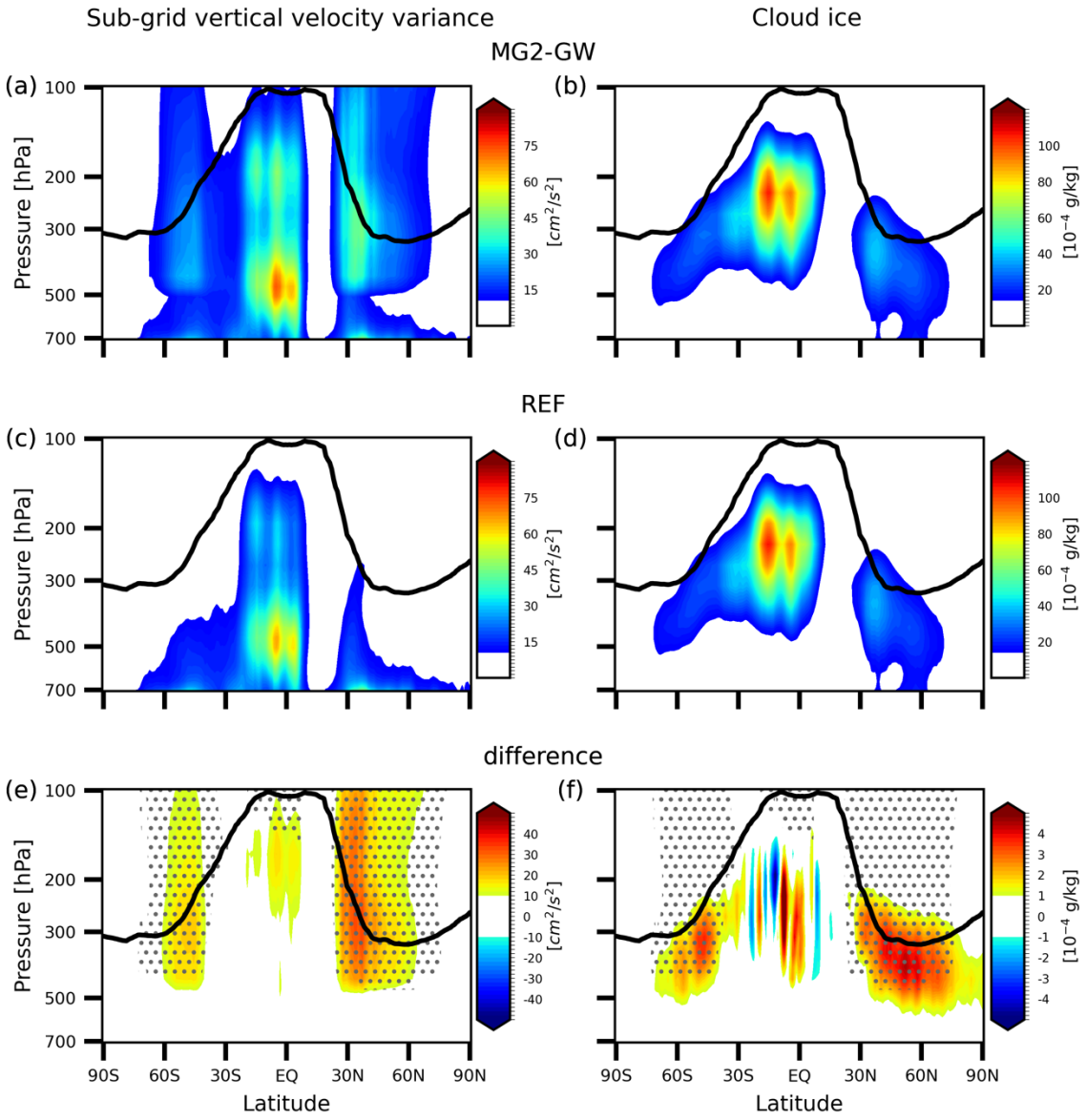

547

548 **Figure 6.** Zonal mean distribution of (left) sub-grid scale vertical velocity variance for ice
549 formation (cm s −1), and (right) grid-box cloud ice amount (kg kg -1) from (top) MG2-GW,
550 (middle) REF, and (bottom) difference between MG2-GW and REF simulations. The results are

551 averaged over January-March. Stippling indicates regions where the relative error with respect to
552 the REF runs exceeds 100%.
553
554
555 **References**
556 Alexander, M., and Coauthors, 2010: Recent developments in gravity-wave effects in climate
557 models and the global distribution of gravity-wave momentum flux from observations and
558 models. Quarterly Journal of the Royal Meteorological Society, 136, 1103-1124.
559 Alpert, J. C., 2004: Sub-grid scale mountain blocking at NCEP. Proceedings of 20th Conference
560 on WAF, 16th conference on NWP, Citeseer.
561 Andrews, D. G., J. R. Holton, and C. B. Leovy, 1987: Middle atmosphere dynamics. Academic
562 press.
563 Barahona, D., A. Molod, and H. Kalesse, 2017: Direct estimation of the global distribution of
564 vertical velocity within cirrus clouds. Scientific Reports, 7, 6840.
565 ——, 2017: Direct estimation of the global distribution of vertical velocity within cirrus clouds.
566 Scientific Reports, 7, 6840.
567 Barnett, J., J. Houghton, and J. Pyle, 1975: The temperature dependence of the ozone
568 concentration near the stratopause. Quarterly Journal of the Royal Meteorological Society, 101,
569 245-257.
570 Beres, J. H., M. J. Alexander, and J. R. Holton, 2004: A method of specifying the gravity wave
571 spectrum above convection based on latent heating properties and background wind. Journal of
572 the atmospheric sciences, 61, 324-337.

573 Beres, J. H., R. R. Garcia, B. A. Boville, and F. Sassi, 2005: Implementation of a gravity wave
574 source spectrum parameterization dependent on the properties of convection in the Whole
575 Atmosphere Community Climate Model (WACCM). Journal of Geophysical Research:
576 Atmospheres, 110.
577 Borrmann, S., S. Solomon, J. E. Dye, D. Baumgardner, K. K. Kelly, and K. R. Chan, 1997:
578 Heterogeneous reactions on stratospheric background aerosols, volcanic sulfuric acid droplets,
579 and type I polar stratospheric clouds: Effects of temperature fluctuations and differences in
580 particle phase. Journal of Geophysical Research: Atmospheres, 102, 3639-3648.
581 Brasseur, G. P., and S. Solomon, 2005: Composition and chemistry. Aeronomy of the Middle
582 Atmosphere: Chemistry and Physics of the Stratosphere and Mesosphere, 265-442.
583 Bramberger, M., Alexander, M. J., Davis, S., Podglajen, A., Hertzog, A., Kalnajs, L., ... &
584 Khaykin, S. (2022). First super-pressure balloon-borne fine-vertical-scale profiles in the upper
585 TTL: Impacts of atmospheric waves on cirrus clouds and the QBO. Geophysical Research
586 Letters, 49(5), e2021GL097596.
587 Bushell, A. C., N. Butchart, S. H. Derbyshire, D. R. Jackson, G. J. Shutts, S. B. Vosper, and S.
588 Webster, 2015: Parameterized gravity wave momentum fluxes from sources related to
589 convection and large-scale precipitation processes in a global atmosphere model. Journal of the
590 Atmospheric Sciences, 72, 4349-4371.
591 Carslaw, K., B. Luo, S. Clegg, T. Peter, P. Brimblecombe, and P. Crutzen, 1994: Stratospheric
592 aerosol growth and HNO3 gas phase depletion from coupled HNO3 and water uptake by liquid
593 particles. Geophysical Research Letters, 21, 2479-2482.

Carslaw, K. S., and Coauthors, 1998: Particle microphysics and chemistry in remotely observed mountain polar stratospheric clouds. Journal of Geophysical Research: Atmospheres, 103, 5785-5796.

Carslaw, K. S., and Coauthors, 1998: Increased stratospheric ozone depletion due to mountain-induced atmospheric waves. Nature, 391, 675-678.

Chapman, S., 1930: XXXV. On ozone and atomic oxygen in the upper atmosphere. The London, Edinburgh, and Dublin Philosophical Magazine and Journal of Science, 10, 369-383.

Charron, M., and E. Manzini, 2002: Gravity waves from fronts: Parameterization and middle atmosphere response in a general circulation model. Journal of the Atmospheric Sciences, 59, 923-941.

Chun, H. Y., and Y. H. Kim, 2008: Secondary waves generated by breaking of convective gravity waves in the mesosphere and their influence in the wave momentum flux. Journal of Geophysical Research: Atmospheres, 113.

Corcos, M., Hertzog, A., Plougonven, R., & Podglajen, A. (2021). Observation of gravity waves at the tropical tropopause using superpressure balloons. Journal of Geophysical Research: Atmospheres, 126(15), e2021JD035165.

Crutzen, P. J., 1971: Ozone production rates in an oxygen-hydrogen-nitrogen oxide atmosphere. Journal of Geophysical Research, 76, 7311-7327.

Danabasoglu, G., and Coauthors, 2020: The community earth system model version 2 (CESM2). Journal of Advances in Modeling Earth Systems, 12, e2019MS001916.

Davis, N. A., P. Callaghan, I. R. Simpson, and S. Tilmes, 2022: Specified dynamics scheme impacts on wave-mean flow dynamics, convection, and tracer transport in CESM2 (WACCM6). Atmospheric Chemistry and Physics, 22, 197-214.

617 Dean, S., J. Flowerdew, B. Lawrence, and S. Eckermann, 2007: Parameterisation of orographic
618 cloud dynamics in a GCM. Climate dynamics, 28, 581-597.
619 Dewan, E. á., and Coauthors, 1998: MSX satellite observations of thunderstorm-generated
620 gravity waves in mid-wave infrared images of the upper stratosphere. Geophysical Research
621 Letters, 25, 939-942.
622 Dinh, T., A. Podglajen, A. Hertzog, B. Legras, and R. Plougonven, 2016: Effect of gravity wave
623 temperature fluctuations on homogeneous ice nucleation in the tropical tropopause layer.
624 Atmospheric Chemistry and Physics, 16, 35-46.
625 Dörnbrack, A., M. Leutbecher, R. Kivi, and E. Kyrö, 1999: Mountain-wave-induced record low
626 stratospheric temperatures above northern Scandinavia. Tellus A: Dynamic Meteorology and
627 Oceanography, 51, 951-963.
628 Dütsch, H., 1968: The photochemistry of stratospheric ozone. Quarterly Journal of the Royal
629 Meteorological Society, 94, 483-497.
630 Emmons, L. K., and Coauthors, 2010: Description and evaluation of the Model for Ozone and
631 Related chemical Tracers, version 4 (MOZART-4). Geoscientific Model Development, 3, 43-67.
632 Ern, M., Trinh, Q. T., Preusse, P., Gille, J. C., Mlynczak, M. G., Russell III, J. M., & Riese, M.
633 (2018). GRACILE: A comprehensive climatology of atmospheric gravity wave parameters based
634 on satellite limb soundings. Earth System Science Data, 10(2), 857-892.
635 Fritts, D. C., and M. J. Alexander, 2003: Gravity wave dynamics and effects in the middle
636 atmosphere. Reviews of geophysics, 41.
637 Fritts, D. C., and G. D. Nastrom, 1992: Sources of mesoscale variability of gravity waves. Part
638 II: Frontal, convective, and jet stream excitation. Journal of Atmospheric Sciences, 49, 111-127.

639 Gelaro, R., and Coauthors, 2017: The modern-era retrospective analysis for research and
640 applications. Version.
641 Gettelman, A., and Coauthors, 2010: Global simulations of ice nucleation and ice supersaturation
642 with an improved cloud scheme in the Community Atmosphere Model. Journal of Geophysical
643 Research: Atmospheres, 115.
644 Gettelman, A., and Coauthors, 2019: The whole atmosphere community climate model version 6
645 (WACCM6). Journal of Geophysical Research: Atmospheres, 124, 12380-12403.
646 Gettelman, A., and H. Morrison, 2015: Advanced two-moment bulk microphysics for global
647 models. Part I: Off-line tests and comparison with other schemes. Journal of Climate, 28, 1268-
648 1287.
649 Golaz, J.-C., Larson, V. E., & Cotton, W. R. (2002a). A PDF-based model for boundary layer
650 clouds. Part I: Method and model description. Journal of the Atmospheric Sciences, 59(24),
651 3540–3551.
652 Golaz, J.-C., Larson, V. E., & Cotton, W. R. (2002b). A PDF-based model for boundary layer
653 clouds. Part II: Model results. Journal of the Atmospheric Sciences, 59(24), 3552–3571.
654 Gregory, D., G. Shutts, and J. Mitchell, 1998: A new gravity-wave-drag scheme incorporating
655 anisotropic orography and low-level wave breaking: Impact upon the climate of the UK
656 Meteorological Office Unified Model. Quarterly Journal of the Royal Meteorological Society,
657 124, 463-493.
658 Haefele, A., Hocke, K., Kämpfer, N., Keckhut, P., Marchand, M., Bekki, S., ... & Rozanov, E.
659 (2008). Diurnal changes in middle atmospheric H2O and O3: Observations in the Alpine region
660 and climate models. Journal of Geophysical Research: Atmospheres, 113(D17).

661 Hindley, N. P., Wright, C. J., Hoffmann, L., Moffat-Griffin, T., & Mitchell, N. J. (2020). An 18-
662 year climatology of directional stratospheric gravity wave momentum flux from 3-D satellite
663 observations. Geophysical research letters, 47(22), e2020GL089557.
664 Holt, L. A., M. J. Alexander, L. Coy, A. Molod, W. Putman, and S. Pawson, 2016: Tropical
665 waves and the quasi-biennial oscillation in a 7-km global climate simulation. Journal of the
666 Atmospheric Sciences, 73, 3771-3783.
667 Holton, J. R., 1983: The influence of gravity wave breaking on the general circulation of the
668 middle atmosphere. Journal of Atmospheric Sciences, 40, 2497-2507.
669 Hoskins, B. J., 1982: The mathematical theory of frontogenesis. Annual review of fluid
670 mechanics, 14, 131-151.
671 Huang, F. T., Mayr, H. G., Russell III, J. M., Mlynczak, M. G., & Reber, C. A. (2008). Ozone
672 diurnal variations and mean profiles in the mesosphere, lower thermosphere, and stratosphere,
673 based on measurements from SABER on TIMED. Journal of Geophysical Research: Space
674 Physics, 113(A4).
675 Huang, F., H. Mayr, J. Russell III, and M. Mlynczak, 2014: Ozone and temperature decadal
676 trends in the stratosphere, mesosphere and lower thermosphere, based on measurements from
677 SABER on TIMED. Annales Geophysicae, Copernicus Publications Göttingen, Germany, 935-
678 949.
679 Jensen, E. J., O. B. Toon, L. Pfister, and H. B. Selkirk, 1996: Dehydration of the upper
680 troposphere and lower stratosphere by subvisible cirrus clouds near the tropical tropopause.
681 Geophysical Research Letters, 23, 825-828.

682 Jewtoukoff, V., A. Hertzog, R. Plougonven, A. de la Camara, and F. Lott, 2015: Comparison of
683 gravity waves in the Southern Hemisphere derived from balloon observations and the ECMWF
684 analyses. Journal of the Atmospheric Sciences, 72, 3449-3468.
685 Jiang, J., S. Eckermann, D. Wu, K. Hocke, B. Wang, J. Ma, and Y. Zhang, 2005: Seasonal
686 variation of gravity wave sources from satellite observation. Advances in Space Research, 35,
687 1925-1932.
688 Kärcher, B., and J. Ström, 2003: The roles of dynamical variability and aerosols in cirrus cloud
689 formation. Atmospheric Chemistry and Physics, 3, 823-838.
690 Kim, Y. J., S. D. Eckermann, and H. Y. Chun, 2003: An overview of the past, present and future
691 of gravity-wave drag parametrization for numerical climate and weather prediction models.
692 Atmosphere-Ocean, 41, 65-98.
693 Kinnison, D., and Coauthors, 2007: Sensitivity of chemical tracers to meteorological parameters
694 in the MOZART-3 chemical transport model. Journal of Geophysical Research: Atmospheres,
695 112.
696 Lean, J. L. (1982). Observation of the diurnal variation of atmospheric ozone. Journal of
697 Geophysical Research: Oceans, 87(C7), 4973-4980.
698 Lilly, D., and P. Kennedy, 1973: Observations of a stationary mountain wave and its associated
699 momentum flux and energy dissipation. Journal of Atmospheric Sciences, 30, 1135-1152.
700 Lindzen, R. S., 1981: Turbulence and stress owing to gravity wave and tidal breakdown. Journal
701 of Geophysical Research: Oceans, 86, 9707-9714.
702 Lindzen, R. S., and J. R. Holton, 1968: A theory of the quasi-biennial oscillation. Journal of
703 Atmospheric Sciences, 25, 1095-1107.

Lyu, K., X. Liu, J. Bacmeister, X. Zhao, L. Lin, Y. Shi, and O. Sourdeval, 2023: Orographic cirrus and its radiative forcing in NCAR CAM6. Journal of Geophysical Research: Atmospheres, 128, e2022JD038164.

Marsh, D. R., M. J. Mills, D. E. Kinnison, J.-F. Lamarque, N. Calvo, and L. M. Polvani, 2013: Climate change from 1850 to 2005 simulated in CESM1 (WACCM). Journal of climate, 26, 7372-7391.

McFarlane, N., 1987: The effect of orographically excited gravity wave drag on the general circulation of the lower stratosphere and troposphere. Journal of the atmospheric sciences, 44, 1775-1800.

McKenna, D., and Coauthors, 1990: Calculations of ozone destruction during the 1988/89 Arctic winter. Geophysical Research Letters, 17, 553-556.

Meilinger, S., and Coauthors, 1995: Size-dependent stratospheric droplet composition in lee wave temperature fluctuations and their potential role in PSC freezing. Geophysical research letters, 22, 3031-3034.

Miller, J. E., 1948: On the concept of frontogenesis. Journal of the Atmospheric Sciences, 5, 169-171.

Mills, M. J., and Coauthors, 2016: Global volcanic aerosol properties derived from emissions, 1990–2014, using CESM1 (WACCM). Journal of Geophysical Research: Atmospheres, 121, 2332-2348.

Nastrom, G. D., and D. C. Fritts, 1992: Sources of mesoscale variability of gravity waves. Part I: Topographic excitation. Journal of the Atmospheric Sciences, 49, 101-110.

Nicolet, M., 1972: Aeronomic chemistry of the stratosphere. Planetary and Space Science, 20, 1671-1702.

O'sullivan, D., and T. J. Dunkerton, 1995: Generation of inertia–gravity waves in a simulated life cycle of baroclinic instability. Journal of Atmospheric Sciences, 52, 3695-3716.

Orr, A., and Coauthors, 2020: PSCs initiated by mountain waves in a global chemistry-climate model: A missing piece in fully modelling polar stratospheric ozone depletion. Atmospheric Chemistry and Physics, 20, 1-15.

Penner, J. E., C. Zhou, A. Garnier, and D. L. Mitchell, 2018: Anthropogenic aerosol indirect effects in cirrus clouds. Journal of Geophysical Research: Atmospheres, 123, 11,652-611,677.

Peter, T., R. Müller, P. J. Crutzen, and T. Deshler, 1994: The lifetime of leewave-induced ice particles in the Arctic stratosphere: II. Stabilization due to NAT-coating. Geophysical research letters, 21, 1331-1334.

Piani, C., D. Durran, M. Alexander, and J. Holton, 2000: A numerical study of three-dimensional gravity waves triggered by deep tropical convection and their role in the dynamics of the QBO. Journal of the Atmospheric Sciences, 57, 3689-3702.

Potter, B. E., and J. R. Holton, 1995: The role of monsoon convection in the dehydration of the lower tropical stratosphere. Journal of the atmospheric sciences, 52, 1034-1050.

Prather, M. J., 1981: Ozone in the upper stratosphere and mesosphere. Journal of Geophysical Research: Oceans, 86, 5325-5338.

Reboita, M. S., de Souza Ferreira, G. W., Ribeiro, J. G. M., & Ali, S. (2024). Assessment of precipitation and near-surface temperature simulation by CMIP6 models in South America. Environmental Research: Climate, 3(2), 025011.

Richter, J. H., F. Sassi, and R. R. Garcia, 2010: Toward a physically based gravity wave source parameterization in a general circulation model. Journal of the Atmospheric Sciences, 67, 136-156.

750 Richter, J. H., A. Solomon, and J. T. Bacmeister, 2014: On the simulation of the quasi-biennial
751 oscillation in the Community Atmosphere Model, version 5. Journal of Geophysical Research:
752 Atmospheres, 119, 3045-3062.
753 Sakaguchi, K., Leung, L. R., Burleyson, C. D., Xiao, H., & Wan, H. (2018). Role of troposphere-
754 convection-land coupling in the southwestern Amazon precipitation bias of the Community
755 Earth System Model version 1 (CESM1). Journal of Geophysical Research: Atmospheres,
756 123(16), 8374-8399.
757 Sakazaki, T., and Coauthors, 2013: Diurnal ozone variations in the stratosphere revealed in
758 observations from the Superconducting Submillimeter-Wave Limb-Emission Sounder (SMILES)
759 on board the International Space Station (ISS). Journal of Geophysical Research: Atmospheres,
760 118, 2991-3006.
761 Schanz, A., K. Hocke, and N. Kämpfer, 2014: Daily ozone cycle in the stratosphere: global,
762 regional and seasonal behaviour modelled with the Whole Atmosphere Community Climate
763 Model. Atmospheric Chemistry and Physics, 14, 7645-7663.
764 Schoeberl, M., A. Dessler, H. Ye, T. Wang, M. Avery, and E. Jensen, 2016: The impact of
765 gravity waves and cloud nucleation threshold on stratospheric water and tropical tropospheric
766 cloud fraction. Earth and Space Science, 3, 295-305.
767 Tabazadeh, A., R. P. Turco, and M. Z. Jacobson, 1994: A model for studying the composition
768 and chemical effects of stratospheric aerosols. Journal of Geophysical Research: Atmospheres,
769 99, 12897-12914.
770 Tsias, A., A. Prenni, K. Carslaw, T. Onasch, B. Luo, M. Tolbert, and T. Peter, 1997: Freezing of
771 polar stratospheric clouds in orographically induced strong warming events. Geophysical
772 research letters, 24, 2303-2306.

773 Weimer, M., Buchmüller, J., Hoffmann, L., Kirner, O., Luo, B., Ruhnke, R., Steiner, M.,
774 Tritscher, I., and Braesicke, P., 2021: Mountain-wave-induced polar stratospheric clouds and
775 their representation in the global chemistry model ICON-ART, Atmos. Chem. Phys., 21, 9515–
776 9543, https://doi.org/10.5194/acp-21-9515-2021.
777 Weimer, M., and Coauthors, 2023: A Method for Estimating Global Subgrid-Scale Orographic
778 Gravity-Wave Temperature Perturbations in Chemistry-Climate Models. Journal of Advances in
779 Modeling Earth Systems, 15, e2022MS003505.
780 Wright, C. J., 2019: Quantifying the global impact of tropical cyclone-associated gravity waves
781 using HIRDLS, MLS, SABER and IBTrACS data. Quarterly Journal of the Royal
782 Meteorological Society, 145, 3023-3039.
783 Yook. S. (2024). Replication Data and Simulation Setups for: Dataset used to generate figures in
784 "Implementation of sub-grid scale temperature perturbations induced by non-orographic gravity
785 waves in WACCM6" [Dataset]. Harvard Dataverse. https://doi.org/10.7910/DVN/KC3VUQ
786 Zhang, G. J., and N. A. McFarlane, 1995: Role of convective scale momentum transport in
787 climate simulation. Journal of Geophysical Research: Atmospheres, 100, 1417-1426.
788 Zou, L., L. Hoffmann, S. Griessbach, R. Spang, and L. Wang, 2021: Empirical evidence for deep
789 convection being a major source of stratospheric ice clouds over North America. Atmospheric
790 chemistry and physics, 21, 10457-10475.

791
792

Journal of Advances in Modeling Earth Systems

Supporting Information for

Implementation of sub-grid scale temperature perturbations induced by non-orographic gravity waves in WACCM6

Simchan Yook1*, Susan Solomon1, Michael Weimer2, Douglas E. Kinnison3, Rolando Garcia3, and Kane Stone1

1 Department of Earth, Atmospheric and Planetary Sciences, Massachusetts Institute of Technology, Cambridge, MA, USA

2 Institute of Environmental Physics, University of Bremen, Bremen, Germany

3 National Center for Atmospheric Research, Boulder, CO, USA

Contents of this file

Introduction

This supporting information illustrates the following: 1) the gravity wave-induced sub-grid scale temperature fluctuations are not sensitive to the simplification method applied for the peak wave displacement calculation (Fig. S1), 2) the global distribution of temperature perturbations from frontal and convective waves (Fig. S2), 3) ozone variations due to dynamical processes and chemical losses from reactions that are not included in Fig. 4c (Fig. S4), and 4) the results based on the sensitivity experiments run with larger amplitudes of wave-induced perturbations (scaling factor = $\sqrt{3}$; Figs. S3, S5, and S6).

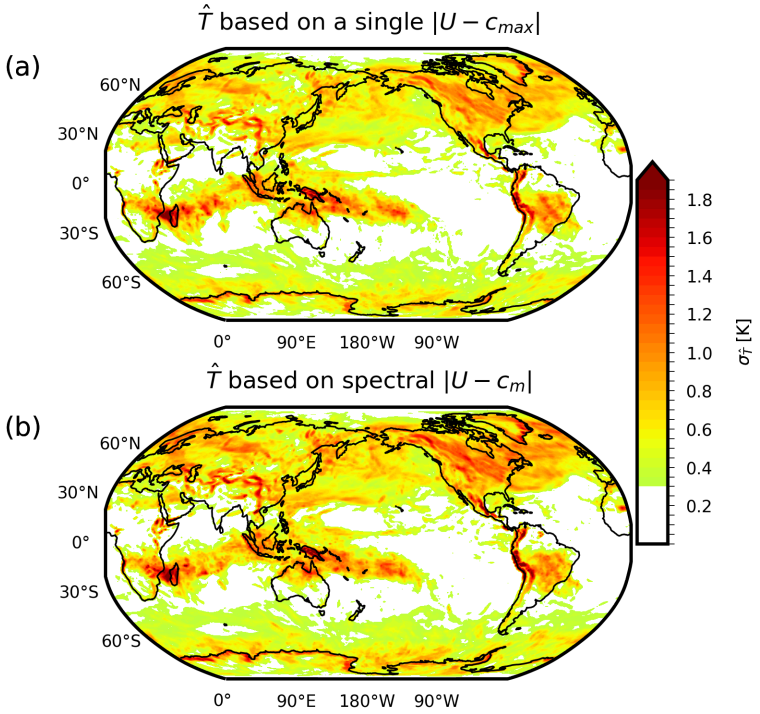

Figure S1. Standard deviation of daily mean $\hat{T}$ at each grid point during 1 January 2007 to 28 February 2007: (a) $\hat{T}$ is estimated using a phase speed of vertical wavenumber (m) corresponding to the maximum momentum flux, and (b) $\hat{T}$ is estimated based on the momentum flux divided by phase speed of each vertical wavenumber.

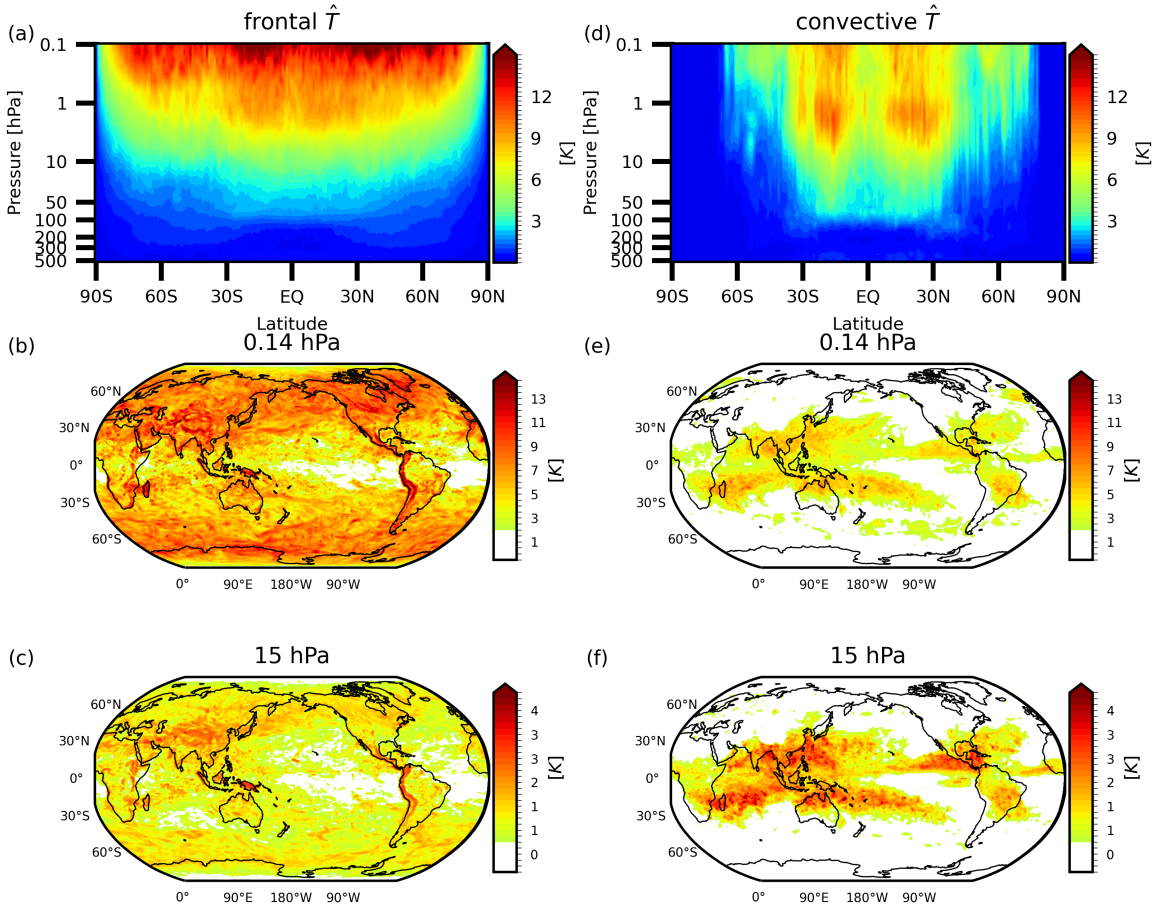

Figure S2. As in Figure 1, but for the temperature perturbations from (left) frontal waves and (right) convective waves.

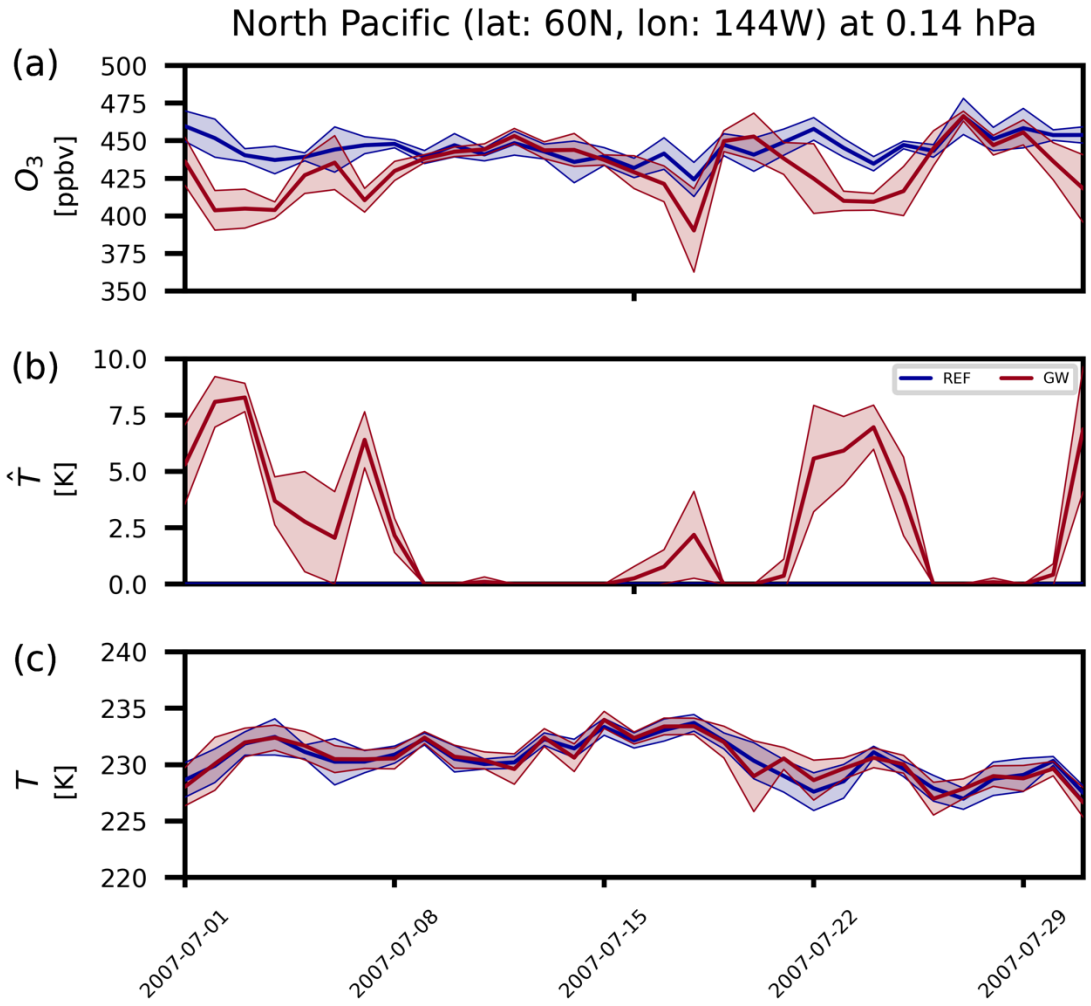

Figure S3. As in Figure 3, but for the results based on the sensitivity experiments run with $\sqrt{3}$ times larger amplitudes of temperature perturbations.

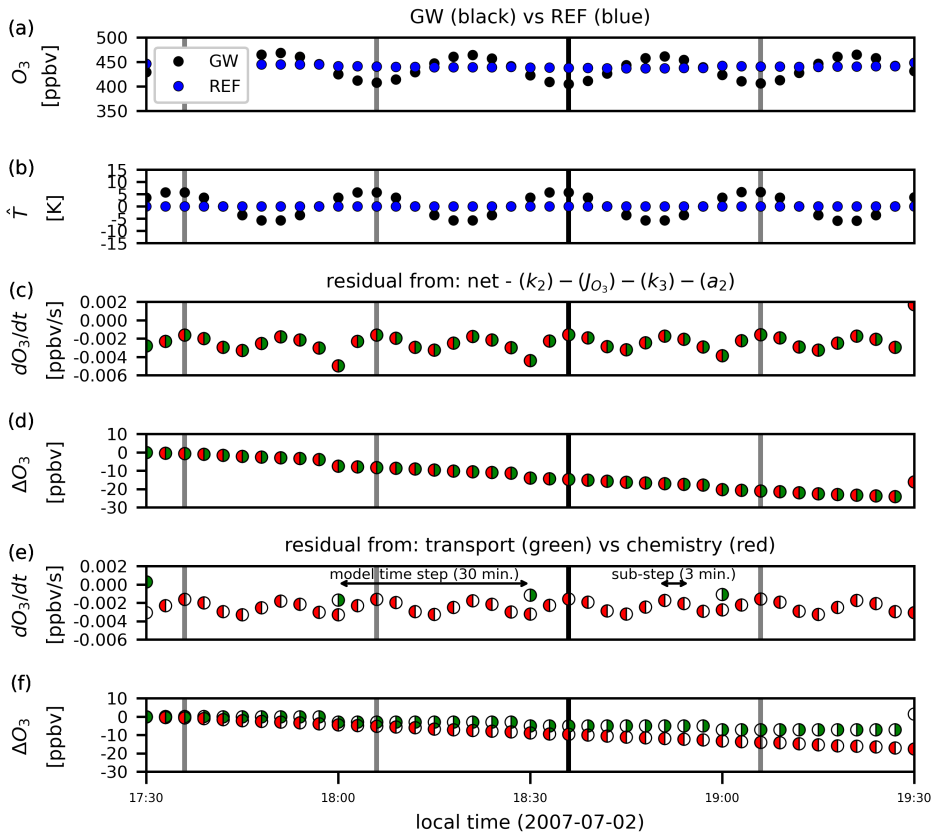

Figure S4. (a) and (b): As in Figs. 4a and 4b, but for black and blue dots representing the GW and REF runs, respectively. (c) and (d): As in Figs. 4c and 4a, but for the difference between 1) the net ozone tendency calculated as the change in ozone mixing ratio between two adjacent sub-time steps, and 2) the net chemical rate shown in Fig. 4c. Thus, the results in panels (c) and (d) represent residual changes in ozone that are not explained by the net chemical rate in Fig. 4c. (e) and (f): As in panels (c) and (d), but separately for residual components due to dynamical transport (green) and other chemical reactions not included in the chemical rate in Fig. 4c (yellow). Thus, the sum of values represented by the green and red circles at each time step in (e) and (f) is equal to the value of each filled circle in (c) and (d), respectively.

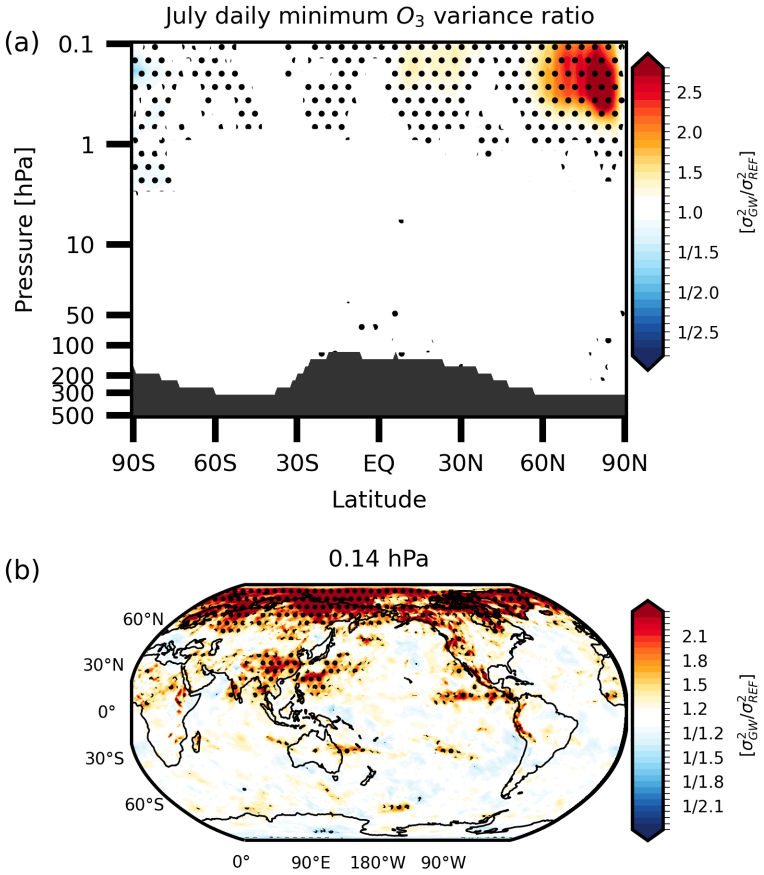

Figure S5. As in Figure 2, but for the results based on the sensitivity experiments run with $\sqrt{3}$ times larger amplitudes of temperature perturbations.

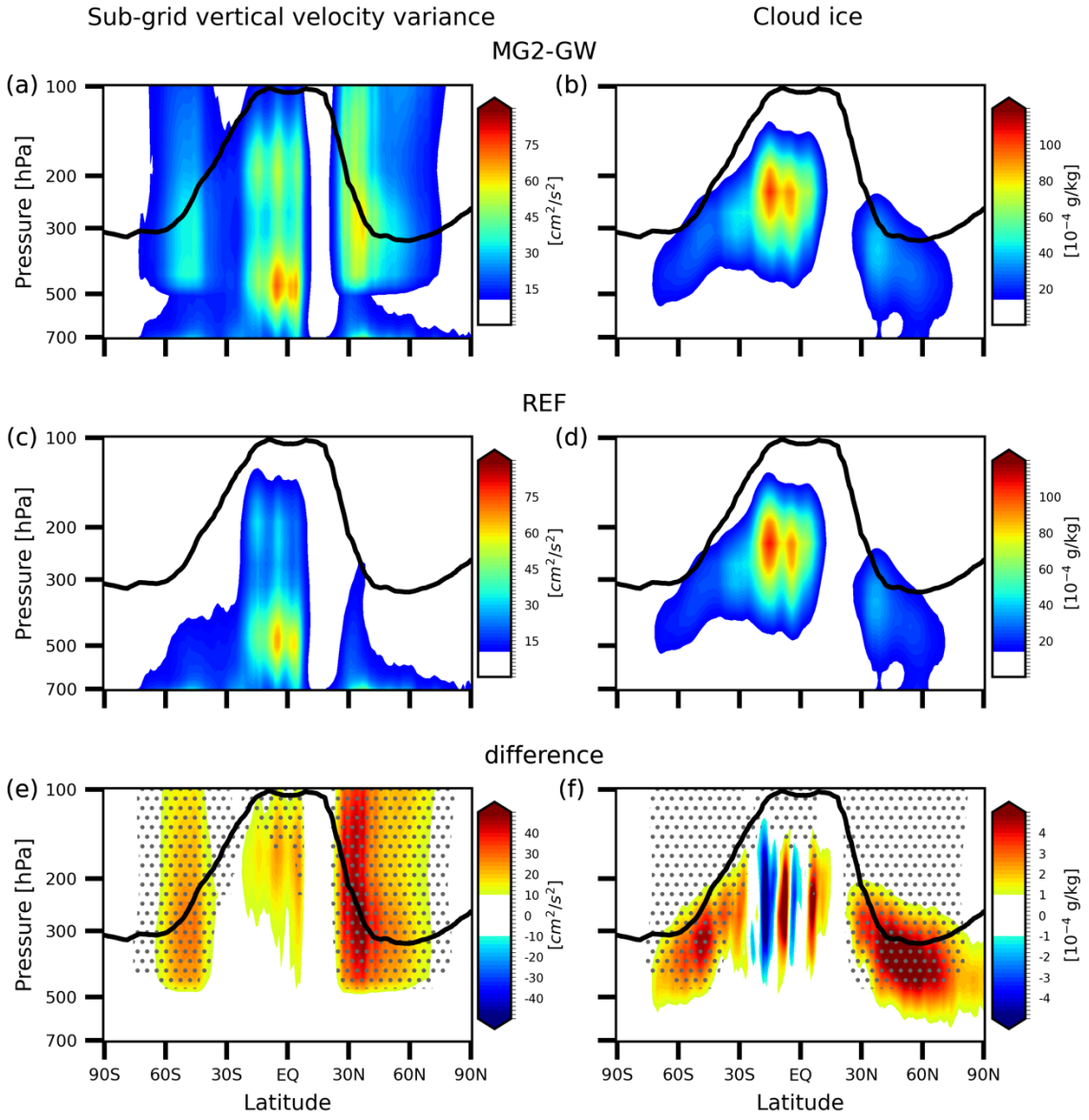

Figure S6. As in Figure 6, but for the results based on the sensitivity experiments run with $\sqrt{3}$ times larger amplitudes of wave-induced vertical velocity perturbations.